nature communications

Article

https://doi.org/10.1038/s41467-024-53879-x

Direct vegetation response to recent CO_2 rise shows limited effect on global streamflow

Received: 20 January 2024

Accepted: 23 October 2024

Published online: 31 October 2024

Check for updates

Haoshan Wei[1,2], Yongqiang Zhang[1] ✉, Qi Huang[1,2], Francis H. S. Chiew[3], Jinkai Luan[1], Jun Xia[4] ✉ & Changming Liu[1]

Global streamflow, crucial for ecology, agriculture, and human activities, can be influenced by elevated atmospheric CO_2 (eCO_2) though direct regulation of vegetation physiology and structure, which can either decrease or increase streamflow. Despite a 21.8% rise in CO_2 over 40 years, its impact on streamflow is not obvious and remains highly debated. Using a full differential approach at the catchment scale and an optimum finger approach globally, both constrained by observed streamflow, here, we find that vegetation responses to eCO_2 in 1981–2020 has limited impact on streamflow via direct regulation. The median eCO_2 contribution approaches zero across 1116 unimpacted catchments, and global streamflow changes cannot be solely attributed to eCO_2. These results offer key insights into the intricate dynamics of CO_2 and other factors shaping streamflow changes over the past four decades. Such understanding is vital for attributing current streamflow changes under eCO_2 conditions.

Streamflow is a vital freshwater resource, an important component of the global water supply[1]. Understanding changes in streamflow and their causation over an extended period is crucial for effective water resources management and availability analysis. Over recent decades, the Earth's land has undergone dramatic climate variations, expected to result in noticeable alterations in streamflow.

Atmospheric CO_2 plays a pivotal role in driving climate change, modulating the global water cycle, and influencing land surface dynamics. Elevated atmospheric CO_2 (eCO_2) can impact changes in streamflow through direct regulation of vegetation physiology and structure[2–8], as well as through indirect effects on radiation and temperature[9–12] that influence precipitation and potential evapotranspiration[4,13–15]. Regarding direct regulation, eCO_2 can induce two major opposing impacts on streamflow: an increasing effect resulting from reduced leaf transpiration due to stomatal closure[3,7,8] and reduced soil evaporation due to expanded leaf area[16,17]. There is also a reducing effect stemming from increased transpiration and intercepted evaporation[6,18] caused by expanded leaf area. Although precipitation, meteorological inputs, and CO_2 concentrations are typically treated as separate inputs in land surface models, the regulation of eCO_2 on climate and associated feedbacks are often integrated into climate change assessments[2,18–23]. Therefore, the impact of eCO_2 on streamflow in this study specifically refers to the direct regulation outlined in Supplementary Fig. 1.

How the eCO_2 influences on streamflow via the direct and indirect regulations, or whether eCO_2 increases or decreases streamflow, remains controversial and uncertain. Some studies emphasize a strong and positive contribution of eCO_2 to increased streamflow due to the water-saving effect caused by stomatal closure[3,7,17,24]. Others indicate that recent global streamflow changes are primarily attributed to climate[2,13,25–27] and land use changes[2,28,29]. Gedney et al. [3] and Piao et al. [2] obtained inconsistent results on streamflow attribution over the last century through different global models, suggesting uncertainty in global modeling[30]. Importantly, a lack of observational support contributes to low confidence in eCO_2 impact modeling results[8,31]. This is mainly because available studies on historical eCO_2 impact on streamflow have focused on the second half of the last century[2,3,28] or before 2010[6,13,32], or on short periods[2,5,24] ranging from one to three

[1]Key Laboratory of Water Cycle and Related Land Surface Processes, Institute of Geographic Sciences and Natural Resources Research, Chinese Academy of Sciences, Beijing 100101, China. [2]University of Chinese Academy of Sciences, Beijing 100049, China. [3]CSIRO Environment, Black Mountain, Canberra ACT 2601, Australia. [4]State Key Laboratory of Water Resources and Hydropower Engineering Sciences, Wuhan University, Wuhan, China.
✉e-mail: zhangyq@igsnrr.ac.cn; xiajun666@whu.edu.cn

https://doi.org/10.1038/s41467-024-53879-x

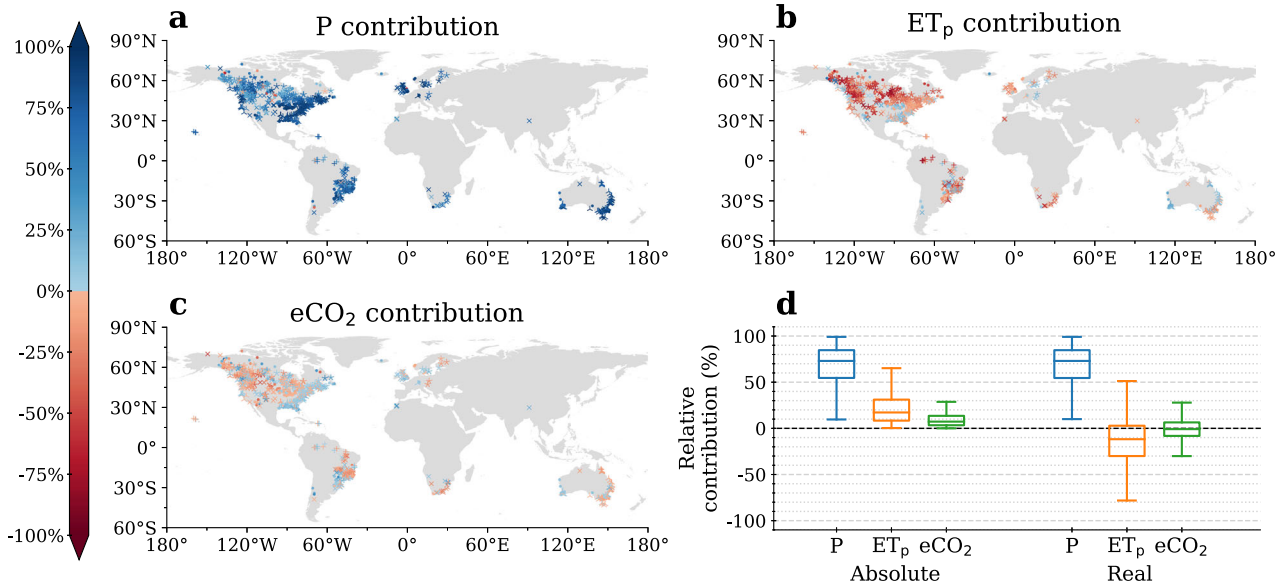

Fig. 1 | Contributions of precipitation (P), potential evapotranspiration (ET_p), and elevated atmospheric CO_2 concentration (eCO_2) to streamflow changes across 1116 unregulated catchments during the period 1981–2020. a Spatial patterns illustrating the relative contribution of precipitation to streamflow. **b** Spatial patterns illustrating the relative contribution of potential evapotranspiration to streamflow. **c** Spatial patterns illustrating the relative contribution of elevated atmospheric CO_2 concentration to streamflow. **d** Box plots showing the relative contributions of the three factors to streamflow across the 1116 catchments. In each box plot, the whiskers represent the 90th and 10th percentiles, and the box is outlined by the 75th, 50th, and 25th percentiles.

decades. Despite a 21.8% increase in atmospheric CO_2 concentration from 1981 to 2020 triggering pronounced global warming[33,34], how vegetation response to eCO_2 influences streamflow at catchment and global scales remains largely unknown. Thus, we aim to utilize a large streamflow dataset along with two state-of-the-art modeling frameworks to unravel the role of eCO_2 in streamflow changes over the past four decades via the direct vegetation regulation.

Results

Catchment scale contributions

We initiated our study by extracting the influences of climate change and eCO_2 on streamflow components from catchments with lengthy observation records, with little human activities in the past 40 years. We employed observed streamflow data from 1116 unimpacted catchments, carefully selected from a vast dataset encompassing over 20,000 catchments worldwide. These specific catchments boast more than 30 years of streamflow observations, exhibit minimal human intervention, and maintain consistent vegetation types (Methods). This unique selection allows us to meticulously disentangle the impacts of precipitation, potential evapotranspiration, and atmospheric CO_2 concentration on streamflow through a fully differential method based on the observed datasets.

The analysis at the catchment scale reveals that precipitation is the primary driver of streamflow changes (Fig. 1a), contributing over 70% to the overall absolute relative contribution (Fig. 1d). While an increase or decrease in precipitation can respectively lead to increases or decreases in streamflow for different catchments, the selected catchments overall exhibit a positive contribution from precipitation (Fig. 1d). Potential evapotranspiration accounts for less than 20% of the absolute relative contribution to overall streamflow changes (Fig. 1d), and in most catchments, it contributes negatively to streamflow changes (Fig. 1b, d).

In contrast, the contribution of eCO_2 to streamflow is considerably lower than that of climate change factors (precipitation and potential evapotranspiration), as depicted in Fig. 1d. The absolute relative contribution of eCO_2 is less than 8% overall, with a median real relative contribution close to 0. No clear statistical evidence shows that eCO_2 provides either a positive or negative contribution to streamflow overall (Fig. 1d). Moreover, the contribution of eCO_2 to streamflow shows certain spatial pattern (Fig. 1c). For example, eCO_2 in southeastern North America shows an overall positive contribution to streamflow, while eCO_2 in eastern Oceania shows an overall negative contribution to streamflow.

Global scale attribution

Subsequently, we employed 14 global ecological models, which were simulated based on observed annual streamflow constraint scenarios of large basins. We then derived four observationally constrained models for our analysis, attribution, and uncertainty studies on global streamflow changes. The regularized optimal fingerprinting method (ROF) was applied for streamflow attribution, utilizing a dataset of pre-industrial revolution-controlled streamflow variability from 47 Earth System Models to represent internal variability. The ROF is a statistical method for attribution by evaluating the internal variability of streamflow and combining it with the statistical relationship between changes in streamflow itself and changes in streamflow driven by external forcing variables to obtain a "fingerprint" or a scale factor. In this paper, an uncertainty analysis was also conducted to evaluate internal variability using different datasets (see Methods).

The attribution analysis results indicate that global streamflow remains relatively stable overall, evident in both the global trend pattern and the area-weighted streamflow trend. More than 80% of global grids exhibit a non-significant increase in streamflow trends, with less than 5% showing a significant change (Fig. 2a). The global area-weighted streamflow displays a non-significant increase, with a trend of $0.09 \pm 0.05\,mm/yr^2$ over the last 40 years (Fig. 2b). Excluding deserts for the global average obtains a similarly non-significant increase trend of $0.13 \pm 0.05\,mm/yr^2$ (Supplementary Fig. 9b). In essence, the globally insignificant changes in streamflow are attributed exclusively to climate change, with no compelling evidence supporting a significant impact of eCO_2 on streamflow.

In Fig. 2c, the scale factor for climate change exhibits strong consistency in both single and multifactor cases, consistently greater than 0 and inclusive of 1. This suggests that the annual changes in streamflow over the past 40 years can be consistently and reliably attributed to climate change (also in Supplementary Fig. 17). However,

https://doi.org/10.1038/s41467-024-53879-x

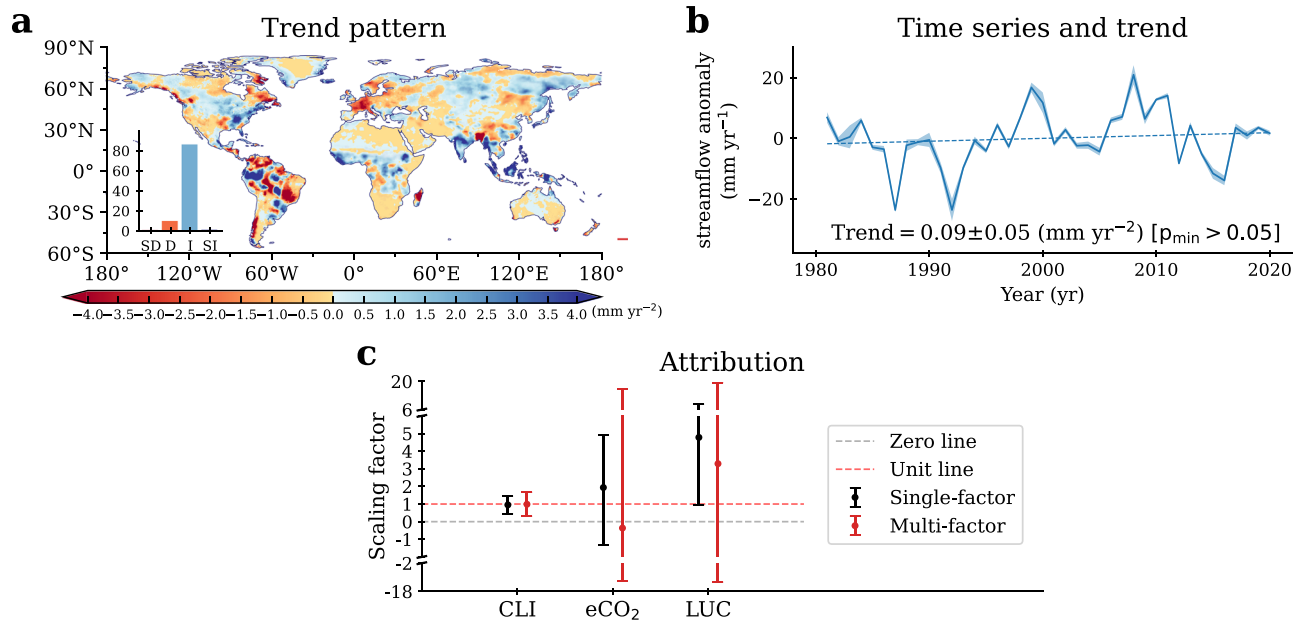

Fig. 2 | Trends, changes and attribution of global streamflow based on observation-constrained models in 1981-2020. a Spatial pattern of 40-year streamflow annual trends obtained from four observation-constrained models. SD, D, I, SI denote significant decrease, insignificant decrease, insignificant increase, and significant increase at the significant level of α = 0.05 (Mann–Kendall test), respectively. Purple dots in global map indicate that the trend is significant. **b** 40-year global area-weighted anomaly streamflow time series and trends for the four observation-constrained models (mean ± 1std), and p_{min} represents the minimum *p* value from the four models. **c** Attribution results for global area-weighted streamflow changes for the four observation-constrained models, with 90% upper and lower bounds and median values for the scale factor of the regularized optimal fingerprinting method being the median of the corresponding values for the four models. If the range of the scale factor at the 90% significance level is greater than 0 and contains 1, the driving factor (climate change (CLI), elevated CO_2 (eCO_2), and land-use change (LUC)) can be attributed; otherwise, it cannot.

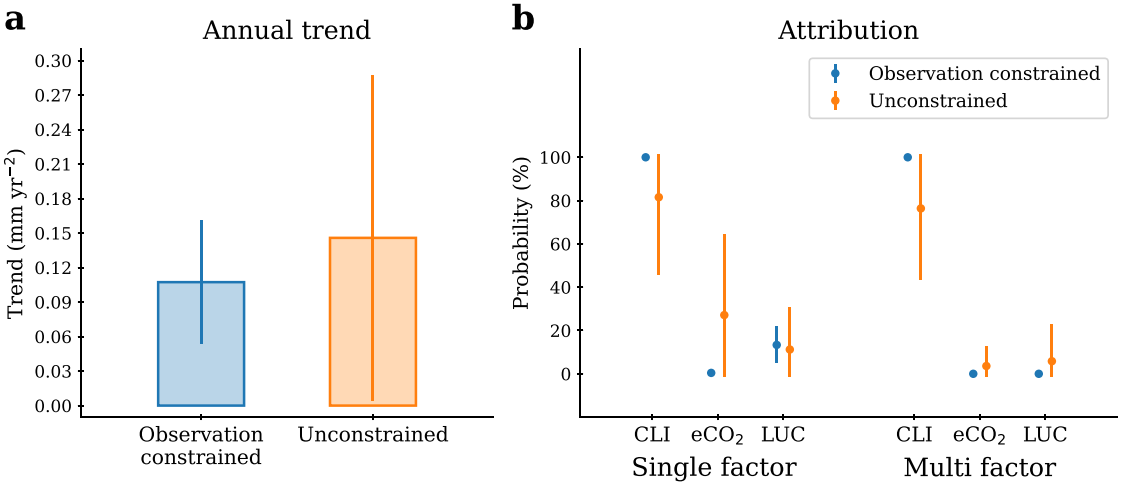

Fig. 3 | Global comparison of annual trend and attribution uncertainty. a Estimates of global streamflow trends. Observed modeling is the mean ± 1 std of the trends from the four observation-constrained models, and the unconstrained is the mean ± 1 std of the trends from the 14 global ecological models. **b** Probabilities of attributing global streamflow to climate change (CLI), elevated CO_2 (eCO_2), and land-use change (LUC) for observation-constrained modeling and all models in TRENDY when different datasets are selected to assess the internal variability of streamflow. The bar error in (**b**) is the one standard deviation of a truncated normal distribution, ranging in 0–100%.

eCO_2 and land-use change cannot be reliably linked to these streamflow changes, especially in the multifactor case. In the multifactor scenario, the scale factors for these two variables fluctuate drastically, implying that their impact on streamflow is much less significant than their influence on climate change.

Uncertainty analysis

Utilizing observation-constrained modeling significantly diminishes the uncertainty inherent in the original 14 models when estimating global streamflow trends and attribution results. Initial estimates of streamflow trends from these models exhibit considerable variation, with some suggesting a noteworthy increase in global streamflow and one model proposing a decline, covering a range of −0.20 to 0.40 mm/yr² (Supplementary Fig. 2). The application of observation-constrained modeling effectively reduces this uncertainty, achieving a 62.0% reduction in standard deviation. This results in a more precise and stable trend estimate (Fig. 3a).

In the application of the optimal fingerprinting method, the choice of diverse datasets for internally assessing global streamflow introduces significant uncertainty into the attribution results across all

the TRENDY models (Fig. 3b). There exists a probability of attributing a change in global streamflow either to eCO_2 or not attributing it to climate change. However, when utilizing the observation-constrained results, the change in global streamflow consistently attributes to climate change but not to eCO_2. This highlights a substantial reduction in uncertainty in the attribution results.

Discussion

Our study uses two frameworks to investigate the impacts of the recent rise in CO_2 on streamflow, focusing on direct vegetation regulation with different considerations. At the small catchment scale, we use the fully differential method, which is not specifically designed to isolate the effects of land-use change on streamflow. Therefore, we carefully select stable catchments that are minimally affected by anthropogenic impacts and vegetation type changes, while also excluding potential impacts of groundwater-streamflow interactions[35]. At the global scale, we use the optimal fingerprinting method to isolate the impacts of eCO_2, climate change, and land-use change on global streamflow. Both frameworks show robust results, indicating that vegetation responses to the recent rise in CO_2 exert limited impacts on streamflow at both catchment and global scales.

It is worth noting that neither of the two frameworks has the capability to investigate the response of climate variables (e.g., precipitation) to vegetation feedback under eCO_2. On one hand, variables such as precipitation are used as forcing data for land-surface and statistical models, and vegetation feedback is embedded within climate forcing. On the other hand, it is challenging to validate the accuracy of vegetation feedback simulations based on observations. These limitations restrict our study to investigating how eCO_2 has influenced streamflow changes over the past four decades through direct vegetation regulation.

We notice that several factors contribute to the uncertainty of the increment-based fully differential method for small catchments (see Methods), including catchment selection and multicollinearity issues among the driving factors, model structural errors and uncertainty in forcing and training datasets. The uncertainty in the fully differential method increases with the size of the catchment area (Supplementary Fig. 10). Larger catchments are more susceptible to anthropogenic change impacts. In our study, more than 74% of the selected catchments have a catchment area of less than 2000 km^2, indicating that the majority of catchments have a low likelihood of experiencing strong anthropogenic changes. In the small catchments, it is also impossible to completely eliminate the anthropogenic impacts. Furthermore, precipitation, potential evapotranspiration, and eCO_2 used in the fully differential method are relatively independent, and there are no collinearity issues[36], as indicated by Variance Inflation Factor values of less than 5.0 (Supplementary Fig. 11). We also notice that the possible impacts from streamflow observation errors that largely vary from 3% to 6%[37–40]. To test the impact magnitude, we conduct the Monte Carlo simulations (see Supplementary Method 4), and find the impact is very small. Specifically, the 10% maximum streamflow error produces an uncertainty in contribution of eCO_2 less than 0.5% for 50% of the selected catchments and less than 0.6% for 75% of the selected catchments (Supplementary Fig. 18). Compared to that, the errors in precipitation generate slightly higher uncertainty in annual streamflow, but it is smaller than the reported precipitation-streamflow error propagation simulated using a process-based hydrological model[41]. Based on the uncertainty analysis, we suggest that the fully differential approach is applicable and robust.

The spatial pattern of eCO_2 contribution to streamflow depicted in Fig. 1c can be attributed to vegetation types (density) and climate regimes. We observed that in forest-dominated catchments with a high leaf area index (as detailed in the Methods), eCO_2 exhibits an overall positive contribution to streamflow in North America (Supplementary Fig. 12a), an overall negative contribution in Oceania (Supplementary Fig. 12c), and a transition from an overall negative to a positive contribution in South America (Supplementary Fig. 12b). In catchments dominated by various vegetation types, the absolute relative contribution of eCO_2 to streamflow in tropical regimes is generally higher than in temperate and cold climate regimes (see Supplementary Fig. 3). However, despite the above discussion, the contribution of eCO_2 to streamflow remains very limited, with an absolute relative contribution of about 10% or less for the selected catchments, and an overall relative contribution close to 0 (Fig. 1d, Supplementary Fig. 3 and Supplementary Fig. 12d). This is far behind precipitation and potential evapotranspiration.

Furthermore, we investigated whether considering vegetation phenology would noticeably impact our results. We focused on catchments outside the equator and conducted the same analysis but only for vegetation growing seasons (April to October for the Northern Hemisphere and October to April for the Southern Hemisphere). The results obtained from the growing seasons mirrored those obtained from the entire calendar year (see Supplementary Fig. 13), further affirming the robustness of our findings.

In the global models, the direct impact of eCO_2 on streamflow is influenced by two opposing factors. On one hand, an increase in vegetation water use efficiency due to eCO_2 can lead to a direct increase in streamflow, as dictated by the stomatal conductance equation in the models[42–45]. Conversely, eCO_2 is a dominant factor in global greening[18], causing an expansion in leaf area and consequently an increase in vegetative water consumption, ultimately reducing streamflow[6]. The substantial eCO_2 levels observed from 1981 to 2020, coupled with the overall insignificant increase in annual streamflow and the minimal attribution of eCO_2 to streamflow (in Fig. 2, and the same results are in the non-desert region, as shown in Supplementary Fig. 9), suggest that the response of global streamflow change to eCO_2 is highly limited, which may be attributed to several factors. Firstly, the effects of global greening and stomatal closure may counteract each other at a regional to global scale. Secondly, the impacts of eCO_2 on vegetation could be relatively small. Thirdly, complex feedback mechanisms remain poorly understood, although observation-constrained models show that the interactive effects of eCO_2 and climate change on streamflow (see Methods) are of the same order of magnitude as the effects of eCO_2 on streamflow, and both are much smaller than the effects of climate change on streamflow (Supplementary Fig. 19).

We also analyze trends in individual water balance components over the past 40 years based on the TRENDY models. These models obtain overall the increasing trends in global evapotranspiration and streamflow, but have a large range in their values. Furthermore, there exists a high uncertainty in these models for partitioning evapotranspiration comments: transpiration, canopy evaporation, and soil evaporation (Supplementary Fig. 20). However, these models achieve reasonable balance in the water balance trends, i.e. trends in precipitation similar to the sum of trend in streamflow and trend in evapotranspiration (Supplementary Figs. 20, 21). These models show the competing effects between the trend in streamflow and the trend in evapotranspiration, i.e. a high trend in streamflow companied by a low trend in evapotranspiration, and vice versa.

While all models successfully simulate annual variability in streamflow when compared to observations (Supplementary Fig. 4b), significant uncertainty persists in trends and attribution results at a global scale (Fig. 3). The application of observational constraints can substantially reduce uncertainty among different models[46]. However, it is important to acknowledge the challenge in achieving high accuracy in both simulated streamflow interannual trends and variations (Supplementary Fig. 4b, c). Constraining models based solely on streamflow variability might lead to higher estimates of global trends (Supplementary Fig. 2). This realization underscores the importance of not only constraining models based on annual streamflow values but also considering annual streamflow trends. The global model

uncertainty on a broad scale underscores the need for cautious assessments of streamflow changes[14].

Methods

Observed streamflow data and forcing data

We utilized annual streamflow data from a comprehensive dataset comprising over 20,000 catchments, gathered from publicly available sources[47–53] and national statistical bulletins. A subset of 1116 small to medium catchments and 44 large basins were chosen for our study. To align with our research objectives, specific criteria were applied to select 1116 unimpacted catchments: catchment areas below 100,000 km², land use/vegetation types area changes under 5% (dataset from HILDA+ (HIstoric Land Dynamics Assessment +)[54,55] including: urban areas, cropland, pasture/rangeland, forest, unmanaged grass/shrubland, and sparse/no vegetation), absence of reservoir regulation (reservoir capacity divided by multi-year average streamflow is 0), irrigated area less than 5% (Global Map of Irrigation Areas (GMIA), https://www.fao.org/land-water/land/land-governance/land-resources-planning-toolbox/category/details/en/c/1029519/), consistent vegetation types, and continuous observations spanning over 30 years (see Supplementary Fig. 5a). Among these catchments, 48.7% had an area less than 500 km², 25.4% ranged between 500 and 2000 km², 18.6% fell between 2000 and 10,000 km², and 7.3% exceeded 10,000 km². To strengthen our results, we further excluded catchments with abrupt shifts in runoff coefficients, resulting in 550 catchments. Details are provided in Supplementary Method 1 and Supplementary Fig. 14, and the corresponding results are summarized in Supplementary Fig. 15, which is similar to the results presented in Fig. 1.

Additionally, 44 large basins, each larger than 100,000 km², were selected having good data availability (each having no less than 36 years of observation and more than 90% catchments with missing percentage less than 1%) (see Supplementary Data 1 for details), covering 24.3% of the global land area (see Supplementary Fig. 5b). For the large basins, missing monthly data were interpolated through the G-RUN dataset[56], subject to a Nash-Sutcliffe efficiency threshold[57] of not less than 0.6 for non-missing months in both G-RUN and these catchments. Basins failing this criterion were excluded, and the boundaries of large basins were separately delineated[58].

Climate classifications are derived from the Köppen-Geiger climate classification maps[59]. A catchment is considered to have a consistent vegetation type if the percentage of one vegetation type is greater than 50% for all 40 years of the catchment. A catchment is dominated by a particular climate or vegetation type if that climate or vegetation type constitutes the largest portion of the catchment. Three types of reservoir data were used in the screening of the 1116 catchments: Basin ATLAS[60], GRanD V1.3[61], and GDAT[62]. Reservoir impacts were calculated by dividing the reservoir flow by the average multi-year streamflow in the catchment, with a reservoir impact of 0 indicating the absence of reservoir regulation. Precipitation and potential evapotranspiration for the fully differential method were sourced from MSWEP V2.8[63] and MSWX[64]. Leaf area index data were sourced from GIMMS3g_V4_1[65].

Trend analysis

Trends were determined using the robust Sen-slope estimator[66], known for its resilience against outliers. The significance of the trends was assessed through the Mann-Kendall test[67,68]. A trend was deemed significant if the p value of the statistical test was less than 0.05; otherwise, the trend was considered not significant.

Fully differential method for catchment scale contribution analysis

We have developed a fully differential method to assess the contributions of eCO_2 and climate change to streamflow. The observed streamflow (Q_{obs}) within a catchment is expressed as a function of hydroclimatic variables (Eq. (1)):

$$Q_{obs} = F(X_1, X_2, \cdots, X_n) \tag{1}$$

where $X_i (i = 1, 2, \cdots, n)$ denotes hydroclimatic variables. The fully differential form for streamflow increment is represented as:

$$dQ = \sum_i \frac{\partial F}{\partial X_i} dX_i \tag{2}$$

where dX_i is the increment in the driving variable. We hypothesize that streamflow trends primarily result from three key drivers: annual precipitation (P), annual potential evapotranspiration (ET_p), and annual CO_2 (CO_2). We approximate Eq. (2) with the annual increments of the regression variables through a standardized multiple regression process (Eq. (3)):

$$\left\{\Delta q_j\right\}_{j\in N} = \sum_i k_i \left\{\Delta x_{i,j}\right\}_{j\in N} + \delta \tag{3}$$

where $\left\{\Delta q_j\right\}_{j\in N}$ is the time series of the standardized streamflow increment, j is time point and N is the natural number indicator set, similarly, $\left\{\Delta x_{i,j}\right\}_{j\in N}$ is the time series of the standardized i-th driving variable increment, k_i is the standardized regression coefficient of the i-th driving variable increment, δ is the uncertainty term. For a given variable $\left\{\hat{x}_{i,j}\right\}_{j\in N}$, the increment is calculated as $\Delta\hat{x}_{i,j} = \hat{x}_{i,j+1} - \hat{x}_{i,j}$ and the normalization process is $\Delta x_{i,j} = \frac{\Delta\hat{x}_{i,j} - \mathrm{MEAN}\left(\left\{\Delta\hat{x}_{i,j}\right\}_{j\in N}\right)}{\mathrm{STD}\left(\left\{\Delta\hat{x}_{i,j}\right\}_{j\in N}\right)}$. It is noted that MEAN and STD are mean and standard deviation, respectively. By performing standardized linear regressions relating annual increments in these dominant factors to annual streamflow increments, we obtain regression coefficients for annual precipitation (k_P), annual potential evapotranspiration (k_{ET_p}), and annual CO_2(k_{CO_2}). The standardized regression coefficients represent the relative contribution of the independent variables to the dependent variable, and trends are an expression of the accumulation of "increments". Therefore, the streamflow changes driven by each factor (X_i) can be expressed as $dQ_{obs\_X_i} = k_{X_i} \cdot \left|\mathrm{Trend}(Q)\right|$, and CO_2-driven streamflow changes are

$$\Delta Q_{obs\_CO_2} = k_{CO_2} \cdot \left|\mathrm{Trend}(Q)\right| \tag{4}$$

where Trend(·) is the trend of the annual variable. The absolute relative contribution and real relative contribution are calculated according to the formula: $|\Delta Q_{obs\_X_i}| / (|\Delta Q_{obs\_P}| + |\Delta Q_{obs\_ET_p}| + |\Delta Q_{obs\_CO_2}|)$, $\Delta Q_{obs\_X_i} / (|\Delta Q_{obs\_P}| + |\Delta Q_{obs\_ET_p}| + |\Delta Q_{obs\_CO_2}|)$, respectively.

The reliability of the method is confirmed by goodness-of-fit (R^2) spatial map and cumulative distribution figures (Supplementary Fig. 6a, b). R^2 in 75% catchments is greater than 0.55, and in 50% catchments is greater than 0.7. Additionally, potential evapotranspiration is calculated using the improved FAO Penman Monteith method (FAO Penman Monteith [Yang])[17], and the results from different potential evapotranspiration formulas exhibit extremely similar correlation coefficients and goodness-of-fit in Eq. (3), as shown in Supplementary Fig. 7. In addition, we evaluate the multicollinearity issue among the driving factors by the Variance Inflation Factor (VIF), where VIF less than 5 is considered to have no multicollinearity among the variables and VIF greater than 10 indicates a strong multicollinearity[36]. The expressions of the equations for the fully differential method and the elasticity coefficient method[14,69] are similar.

In contrast to the elasticity coefficient method, the fully differential method requires the consideration of all potential driving variables, which is the key reason for the rigorous screening of the catchments.

Global ecological models

We employed 14 state-of-the-art process-based global ecological models to assess and attribute streamflow changes, obtained from latest TRENDY phase 11[21,70]. These models, including CABLE-POP[71], CLASSIC[72], CLM5.0[73], DLEM[74], IBIS[75], ISAM[76], ISBA-CTRIP[77], JSBACH[78], JULES[79,80], LPJ-GUESS[81], LPX-BERN[82], ORCHIDEE[83], SDGVM[84] and VISIT-NIES[85], are widely used for evaluating hydrological effects and attributions[2,22,86].

The model results were provided through the TRENDY project (https://sites.exeter.ac.uk/trendy), specifically from the S3 scenario simulations, which consider all forcing data (eCO_2, climate change, and land use change) as time-varying and are deemed to be most representative of the real world[18,22]. Half of these models have a spatial resolution of 0.5°×0.5°. To facilitate calculations, all model results were resampled to a spatial resolution of 0.5°×0.5° using bilinear interpolation, as needed, for consistency in spatial representation. Model details are summarized in Supplementary Method 3 and Supplementary Data 2.

Using TRENDY model experiments, we can partition the trend in streamflow into three components: CO_2-driven, climate-driven, and interactive effects of climate change and CO_2. The CO_2-driven streamflow trend from TRENDY models is:

$$\Delta Q_{CO_2} = \mathrm{Trend}\left(Q_{S1} - Q_{S0}\right) \tag{5}$$

where ΔQ_{CO_2} is the CO_2-driven streamflow trend from TRENDY models; $\mathrm{Trend}(\cdot)$ is the function to calculate the trend, Sen-slope estimator is used here; Q_{S0}, Q_{S1} are the streamflow from S0, and S1 in the TRENDY control scenarios (see Supplementary Method 3).

The climate-driven streamflow trend from TRENDY models is:

$$\Delta Q_{CLI} = \mathrm{Trend}\left(Q_{S2} - Q_{S1}\right) \tag{6}$$

where ΔQ_{CLI} is the climate-driven streamflow trend from TRENDY models; $\mathrm{Trend}(\cdot)$ is same as Eq. (5); Q_{S2} is the streamflow from S2 in the TRENDY control scenarios (see Supplementary Method 3).

The streamflow trend driven by CO_2 and climate from TRENDY models is:

$$\Delta Q_{CO_2\_CLI} = \mathrm{Trend}\left(Q_{S2} - Q_{S0}\right) \tag{7}$$

where $\Delta Q_{CO_2\_CLI}$ is the streamflow trend driven by CO_2 and climate from TRENDY models; others are same as Eqs. (5) and (6).

Therefore, the streamflow trend driven by the interactive effects of climate change and CO_2 from TRENDY models is:

$$\Delta Q_{\mathrm{Interaction}} = \Delta Q_{CO_2\_CLI} - \Delta Q_{CO_2} - \Delta Q_{CLI} \tag{8}$$

where $\Delta Q_{\mathrm{Interaction}}$ is the streamflow trend driven by the interactive effects of climate change and CO_2 from TRENDY models. The CO_2-driven and climate-driven (combination of precipitation and potential evapotranspiration) streamflow trend calculated by the fully differential method can be deduced from Eq. (4), which corresponds to Eqs. (5) and (6).

Observation-constrained modeling

We developed four observation-constrained models based on the annual observed streamflow values and trends. For each continent, we pursued two approaches: (1) maximizing the Nash-Sutcliffe efficiency (NSE) of the model-simulated annual streamflow series against the observed annual streamflow series to derive the value-constrained models (two types: single, named Best-VAS-SM, and multi-model ensemble, named Best-VAS-EM), and (2) minimizing the Root Minimum Mean Square Error (RMSE) of the model-simulated annual streamflow trend against the observed annual streamflow trend to obtain the trend-constrained models (two types: single, named Best-TAS-SM, and multi-model ensemble, named Best-TAS-EM) (See Supplementary Method 2 for details). The multi-model ensemble models involved an averaging process, followed by an optimization algorithm (Strategic Random Search[87]) to identify optimal values. The results of the model selection are depicted in Supplementary Fig. 4a, and validation of modelled trends for the 44 large basins is shown in Supplementary Fig. 8 and Supplementary Fig. 16.

Regularized optimal fingerprint method for attribution analysis

We employed the optimal fingerprint method (OF) for global attribution analysis, specifically using the regularized OF (ROF), which enhances OF by eliminating the stage parameter determination in the Empirical Orthogonal Function projection. This refinement contributes to increased accuracy[88]. The core equation for ROF remains consistent with OF:

$$y = \sum_{i=1}^{l} \beta_i x_i + \epsilon \tag{9}$$

where y represents the streamflow (obtained from TRENDY models or observation-constrained estimates in this context), x_i is the response to the i-th external forcing variable, derived from the TRENDY control scenarios described in Supplementary Method 3, β_i is an unknown scaling factor, and ϵ denotes the internal streamflow variability, computed from the pre-industrial revolution-controlled (CTL) from the Earth System Models (ESMs) in CMIP6[89] (A total of 47 models were collected, as shown in Supplementary Data 3). y, x_i, and ϵ consist of spatio-temporal vectors. When β_i and its 90% confidence interval are both greater than 0 and contain unity, changes in streamflow can be attributed to the i-th external forcing.

In this study, both single-factor (or single-signal) and multi-factor (or multi-signal) analyses were employed throughout the attribution process. Single-factor analysis provides a quick and simple way to determine whether a variable can be attributed or not. In contrast, multi-factor analysis tests the robustness of the attribution results for a single-factor variable, especially when other variables are added to attribution simultaneously.

However, we observed a heavy reliance of ϵ on the CTL dataset. To construct noisy covariances of internal streamflow variability, we extracted non-overlapping 80-year data blocks (twice the length of 1981–2020) from various available CTLs in the Earth System Models (ESMs) randomly. For each experiment, no less than 24 ESMs were randomly selected through uniform distribution. Each 80-year data block was then split into two 40-year data blocks, from which we calculated the area-weighted annual mean streamflow anomaly. This process yielded two independent matrices, one for determining the noise covariance and the other for testing residual consistency[88,90]. Subsequently, this experiment was repeated 100 times to account for variations in results due to different CTL model selection processes.

To enhance the reliability of the results by reducing temporal dimensions, we chose multi-year non-overlapping means for further calculation. Previous studies often employed means over 3-year[12,18,22], 5-year[91], and 11-year[92] periods. However, due to the limited 40-year streamflow data in this paper, we selected non-overlapping means of 3-year, 4-year, and 5-year durations for the calculation, resulting in a total of 300 sets of results.

If changes in streamflow can be attributed to a variable x_i (climate change, eCO_2, and land use change), then the probability that it can be

attributed is given by:

$$P_{x_i} = \frac{A_{x_i}}{N} \times 100\% \quad (10)$$

where A_{xi} is the number of times that x_i can be attributed, and N is the total number of times, which is 300 in this case.

Data availability

Source data are provided with this paper. More detailed data for our analyses are provided from the following link: https://zenodo.org/records/13908543 [93]. Other publicly available datasets include: the Global Runoff Data Centre (GRDC) (https://www.bafg.de/GRDC/EN/01_GRDC/grdc_node.html); Dai's update streamflow (DAI) (https://rda.ucar.edu/datasets/d551000/); Service d'observation des ressources en eaux du bassin de l'Amazone (SO-HyBam) (https://hybam.obs-mip.fr/); the Catchment Attributes and Meteorology for Large-sample Studies (CAMELS) (https://gdex.ucar.edu/dataset/camels.html); the African Database of Hydrometric Indices (ADHI) (https://dataverse.ird.fr/dataset.xhtml?persistentId=doi:10.23708/LXGXQ9); the China River Sediment Bulletin (CRSB) (http://www.irtces.org/nszx/cbw/hlnsgb/A550406index_1.htm); the Global Streamflow Indices and Metadata Archive (GSIM) (https://doi.pangaea.de/10.1594/PANGAEA.887477); Peterson's streamflow dataset (https://github.com/peterson-tim-j/HydroState/tree/master); the Global Runoff Ensemble (G-RUN) (https://doi.org/10.6084/m9.figshare.12794075); the HIstoric Land Dynamics Assessment+ (HILDA +) (https://doi.pangaea.de/10.1594/PANGAEA.921846?format=html#download). Reservoir data sets: Basin ATLAS; the Global Reservoir and Dam database V1.3 (GRanD V1.3) (https://www.globaldamwatch.org/grand); the Global Dam Tracker (GDAT) (https://doi.org/10.5281/zenodo.6784716); the Köppen-Geiger Climate Classification Maps (https://www.gloh2o.org/koppen/); the Multi-Source Weighted-Ensemble Precipitation V2.8 (MSWEP V2.8) (https://www.gloh2o.org/mswep/); the Multi-Source Weather (MSWX) (https://www.gloh2o.org/mswx/); the Global Inventory Modeling and Mapping Studies LAI3g V4_1 (GIMMS3g_V4_1) (https://ecocast.arc.nasa.gov/data/pub/gimms/); and the Global Map of Irrigation Areas (GMIA) (https://www.fao.org/land-water/land/land-governance/land-resources-planning-toolbox/category/details/en/c/1029519/). Source data are provided with this paper.

Code availability

The codes for the analyses are available at https://zenodo.org/records/13908543 [93].

References

1. Zhang, Y. et al. Southern Hemisphere dominates recent decline in global water availability. *Science* **382**, 579–584 (2023).
2. Piao, S. et al. Changes in climate and land use have a larger direct impact than rising CO_2 on global river runoff trends. *Proc. Natl Acad. Sci. USA.* **104**, 15242–15247 (2007).
3. Gedney, N. et al. Detection of a direct carbon dioxide effect in continental river runoff records. *Nature* **439**, 835–838 (2006).
4. Zhou, S., Yu, B., Lintner, B. R., Findell, K. L. & Zhang, Y. Projected increase in global runoff dominated by land surface changes. *Nat. Clim. Chang.* **13**, 442–449 (2023).
5. Cui, J. et al. Vegetation forcing modulates global land monsoon and water resources in a CO_2-enriched climate. *Nat. Commun.* **11**, 5184 (2020).
6. Ukkola, A. M. et al. Reduced streamflow in water-stressed climates consistent with CO_2 effects on vegetation. *Nat. Clim. Change* **6**, 75–78 (2016).
7. Betts, R. A. et al. Projected increase in continental runoff due to plant responses to increasing carbon dioxide. *Nature* **448**, 1037–1041 (2007).
8. Fowler, M. D., Kooperman, G. J., Randerson, J. T. & Pritchard, M. S. The effect of plant physiological responses to rising CO_2 on global streamflow. *Nat. Clim. Chang.* **9**, 873–879 (2019).
9. Skinner, C. B., Poulsen, C. J. & Mankin, J. S. Amplification of heat extremes by plant CO_2 physiological forcing. *Nat. Commun.* **9**, 1094 (2018).
10. He, M., Lian, X., Cui, J., Xu, H. & Piao, S. Vegetation Physiological Response to Increasing Atmospheric CO_2 Slows the Decreases in the Seasonal Amplitude of Temperature. *Geophys. Res. Lett.* **49**, e2022GL097829 (2022).
11. Park, S.-W., Kim, J.-S. & Kug, J.-S. The intensification of Arctic warming as a result of CO_2 physiological forcing. *Nat. Commun.* **11**, 2098 (2020).
12. Liu, J. et al. Detection and Attribution of Human Influence on the Global Diurnal Temperature Range Decline. *Geophys. Res. Lett.* **49**, e2021GL097155 (2022).
13. Gudmundsson, L. et al. Globally observed trends in mean and extreme river flow attributed to climate change. *Science* **371**, 1159–1162 (2021).
14. Zhang, Y. et al. Future global streamflow declines are probably more severe than previously estimated. *Nat. Water* **1**, 261–271 (2023).
15. Wang, H. et al. Anthropogenic climate change has influenced global river flow seasonality. *Science* **383**, 1009–1014 (2024).
16. Hsu, H. & Dirmeyer, P. A. Soil moisture-evaporation coupling shifts into new gears under increasing CO2. *Nat. Commun.* **14**, 1162 (2023).
17. Yang, Y., Roderick, M. L., Zhang, S., McVicar, T. R. & Donohue, R. J. Hydrologic implications of vegetation response to elevated CO_2 in climate projections. *Nat. Clim. Change* **9**, 44–48 (2019).
18. Zhu, Z. et al. Greening of the Earth and its drivers. *Nat. Clim. Change* **6**, 791–795 (2016).
19. Kooperman, G. J. et al. Forest response to rising CO_2 drives zonally asymmetric rainfall change over tropical land. *Nat. Clim. Change* **8**, 434–440 (2018).
20. Skinner, C. B., Poulsen, C. J., Chadwick, R., Diffenbaugh, N. S. & Fiorella, R. P. The Role of Plant CO_2 Physiological Forcing in Shaping Future Daily-Scale Precipitation. *J. Clim.* **30**, 2319–2340 (2017).
21. Sitch, S. et al. Recent trends and drivers of regional sources and sinks of carbon dioxide. *Biogeosciences* **12**, 653–679 (2015).
22. Liu, J. et al. Response of global land evapotranspiration to climate change, elevated CO_2, and land use change. *Agric. For. Meteorol.* **311**, 108663 (2021).
23. O'Sullivan, M. et al. Process-oriented analysis of dominant sources of uncertainty in the land carbon sink. *Nat. Commun.* **13**, 4781 (2022).
24. Cao, L., Bala, G., Caldeira, K., Nemani, R. & Ban-Weiss, G. Importance of carbon dioxide physiological forcing to future climate change. *Proc. Natl Acad. Sci. Usa.* **107**, 9513–9518 (2010).
25. Alkama, R. et al. Global Evaluation of the ISBA-TRIP Continental Hydrological System. Part I: Comparison to GRACE Terrestrial Water Storage Estimates and In Situ River Discharges. *J. Hydrometeorol.* **11**, 583–600 (2010).
26. Liu, J., You, Y., Zhang, Q. & Gu, X. Attribution of streamflow changes across the globe based on the Budyko framework. *Sci. Total Environ.* **794**, 148662 (2021).
27. Oliveira, P. J. C., Davin, E. L., Levis, S. & Seneviratne, S. I. Vegetation-mediated impacts of trends in global radiation on land hydrology: a global sensitivity study. *Glob. Change Biol.* **17**, 3453–3467 (2011).
28. Yang, H., Huntingford, C., Wiltshire, A., Sitch, S. & Mercado, L. Compensatory climate effects link trends in global runoff to rising atmospheric CO_2 concentration. *Environ. Res. Lett.* **14**, 124075 (2019).
29. Sterling, S. M., Ducharne, A. & Polcher, J. The impact of global land-cover change on the terrestrial water cycle. *Nat. Clim. Change* **3**, 385–390 (2013).
30. Gudmundsson, L., Greve, P. & Seneviratne, S. I. The sensitivity of water availability to changes in the aridity index and other factors—

A probabilistic analysis in the Budyko space. *Geophys. Res. Lett.* **43**, 6985–6994 (2016).
31. Cui, J. et al. Global water availability boosted by vegetation-driven changes in atmospheric moisture transport. *Nat. Geosci.* **15**, 982–988 (2022).
32. Yang, Y. et al. Low and contrasting impacts of vegetation CO_2 fertilization on global terrestrial runoff over 1982–2010: accounting for aboveground and belowground vegetation–CO_2 effects. *Hydrol. Earth Syst. Sci.* **25**, 3411–3427 (2021).
33. Wang, Y.-R., Hessen, D. O., Samset, B. H. & Stordal, F. Evaluating global and regional land warming trends in the past decades with both MODIS and ERA5-Land land surface temperature data. *Remote Sens. Environ.* **280**, 113181 (2022).
34. Kogan, F. Malaria Performance Trend During 1981–2020 Global Warming. In *Remote Sensing Land Surface Changes: The 1981-2020 Intensive Global Warming* (ed. Kogan, F.) 333–371 (Springer International Publishing, Cham, https://doi.org/10.1007/978-3-030-96810-6_10 (2022).
35. Schaller, M. F. & Fan, Y. River basins as groundwater exporters and importers: Implications for water cycle and climate modeling. *J. Geophys. Res.* **114**, D04103 (2009).
36. O'brien, R. M. A Caution Regarding Rules of Thumb for Variance Inflation Factors. *Qual. Quant.* **41**, 673–690 (2007).
37. Sauer, V. B. & Meyer, R. W. Determination of error in individual discharge measurements: U.S. Geological Survey Open-File Report 92–144, 21 p. (1992).
38. Dingman, S. L. *Physical Hydrology, Third Edtion*. (Waveland Press, Long Grove, 2015).
39. Li, X. et al. Evapotranspiration Estimation for Tibetan Plateau Headwaters Using Conjoint Terrestrial and Atmospheric Water Balances and Multisource Remote Sensing. *Water Resour. Res.* **55**, 8608–8630 (2019).
40. Ma, N., Zhang, Y. & Szilagyi, J. Water-balance-based evapotranspiration for 56 large river basins: A benchmarking dataset for global terrestrial evapotranspiration modeling. *J. Hydrol.* **630**, 130607 (2024).
41. Nanding, N. et al. Assessment of Precipitation Error Propagation in Discharge Simulations over the Contiguous United States. *J. Hydrometeorol.* https://doi.org/10.1175/JHM-D-20-0213.1 (2021).
42. Adams, M. A., Buckley, T. N. & Turnbull, T. L. Diminishing CO_2-driven gains in water-use efficiency of global forests. *Nat. Clim. Chang.* **10**, 466–471 (2020).
43. Keenan, T. F. et al. Increase in forest water-use efficiency as atmospheric carbon dioxide concentrations rise. *Nature* **499**, 324–327 (2013).
44. De Kauwe, M. G. et al. Forest water use and water use efficiency at elevated CO_2: a model-data intercomparison at two contrasting temperate forest FACE sites. *Glob. Change Biol.* **19**, 1759–1779 (2013).
45. Guerrieri, R. et al. Disentangling the role of photosynthesis and stomatal conductance on rising forest water-use efficiency. *Proc. Natl Acad. Sci. Usa.* **116**, 16909–16914 (2019).
46. Lehner, F. et al. The potential to reduce uncertainty in regional runoff projections from climate models. *Nat. Clim. Chang.* **9**, 926–933 (2019).
47. BfG - The GRDC. https://www.bafg.de/GRDC/EN/01_GRDC/grdc_node.html.
48. Dai, A. Hydroclimatic trends during 1950–2018 over global land. *Clim. Dyn.* **56**, 4027–4049 (2021).
49. SO-HyBam – Service d'observation des ressources en eaux du bassin de l'Amazone. https://hybam.obs-mip.fr/.
50. Addor, N., Newman, A. J., Mizukami, N. & Clark, M. P. The CAMELS data set: catchment attributes and meteorology for large-sample studies. *Hydrol. Earth Syst. Sci.* **21**, 5293–5313 (2017).
51. Tramblay, Y. et al. ADHI: the African Database of Hydrometric Indices (1950–2018). *Earth Syst. Sci. Data* **13**, 1547–1560 (2021).
52. Do, H. X., Gudmundsson, L., Leonard, M. & Westra, S. The Global Streamflow Indices and Metadata Archive (GSIM) – Part 1: The production of a daily streamflow archive and metadata. *Earth Syst. Sci. Data* **10**, 765–785 (2018).
53. Peterson, T. J., Saft, M., Peel, M. C. & John, A. Watersheds may not recover from drought. *Science* **372**, 745–749 (2021).
54. Winkler, K., Fuchs, R., Rounsevell, M. & Herold, M. Global land use changes are four times greater than previously estimated. *Nat. Commun.* **12**, 2501 (2021).
55. Winkler, K., Fuchs, R., Rounsevell, M. D. A. & Herold, M. HILDA+ Global Land Use Change between 1960 and 2019. PANGAEA https://doi.org/10.1594/PANGAEA.921846 (2020).
56. Ghiggi, G., Humphrey, V., Seneviratne, S. I., & Gudmundsson, L. G-RUN ENSEMBLE: a multi-forcing observation-based global runoff reanalysis. *Water Res. Res.* **57**, e2020WR028787 (2021).
57. Nash, J. E. & Sutcliffe, J. V. River flow forecasting through conceptual models part I — A discussion of principles. *J. Hydrol.* **10**, 282–290 (1970).
58. Xie, J., Liu, X., Bai, P. & Liu, C. Rapid watershed delineation using an automatic outlet relocation algorithm. *Water Res. Rese.* **58**, e2021WR031129 (2022).
59. Beck, H. E. et al. Publisher Correction: Present and future Köppen-Geiger climate classification maps at 1-km resolution. *Sci. Data* **7**, 274 (2020).
60. Linke, S. et al. Global hydro-environmental sub-basin and river reach characteristics at high spatial resolution. *Sci. Data* **6**, 283 (2019).
61. Lehner, B. et al. High-resolution mapping of the world's reservoirs and dams for sustainable river-flow management. *Front. Ecol. Environ.* **9**, 494–502 (2011).
62. Zhang, A. T. & Gu, V. X. Global Dam Tracker: A database of more than 35,000 dams with location, catchment, and attribute information. *Sci. Data* **10**, 111 (2023).
63. Beck, H. E. et al. MSWEP V2 Global 3-Hourly 0.1° Precipitation: Methodology and Quantitative Assessment. *Bull. Am. Meteorological Soc.* **100**, 473–500 (2019).
64. Beck, H. E. et al. MSWX: Global 3-Hourly 0.1° Bias-Corrected Meteorological Data Including Near-Real-Time Updates and Forecast Ensembles. *Bull. Am. Meteorological Soc.* **103**, E710–E732 (2022).
65. Zhu, Z. et al. Global Data Sets of Vegetation Leaf Area Index (LAI)3g and Fraction of Photosynthetically Active Radiation (FPAR)3g Derived from Global Inventory Modeling and Mapping Studies (GIMMS) Normalized Difference Vegetation Index (NDVI3g) for the Period 1981 to 2011. *Remote Sens.* **5**, 927–948 (2013).
66. Sen, P. K. Estimates of the Regression Coefficient Based on Kendall's Tau. *J. Am. Stat. Assoc.* **63**, 1379–1389 (1968).
67. Kendall, M. G. *Rank Correlation Measures*. vol. 15 (Charles Griffin, London, 1975).
68. Mann, H. B. Nonparametric Tests Against Trend. *Econometrica* **13**, 245–259 (1945).
69. Anderson, B. J., Brunner, M. I., Slater, L. J. & Dadson, S. J. Elasticity curves describe streamflow sensitivity to precipitation across the entire flow distribution. *Hydrol. Earth Syst. Sci.* **28**, 1567–1583 (2023).
70. Friedlingstein, P. et al. Global Carbon Budget 2022. *Earth Syst. Sci. Data* **14**, 4811–4900 (2022).
71. Haverd, V. et al. A new version of the CABLE land surface model (Subversion revision r4601) incorporating land use and land cover change, woody vegetation demography, and a novel optimisation-based approach to plant coordination of photosynthesis. *Geosci. Model Dev.* **11**, 2995–3026 (2018).
72. Melton, J. R. et al. CLASSIC v1.0: the open-source community successor to the Canadian Land Surface Scheme (CLASS) and the Canadian Terrestrial Ecosystem Model (CTEM) – Part 1: Model

framework and site-level performance. *Geoscientific Model Dev*. **13**, 2825–2850 (2020).
73. Lawrence, D. M. et al. The Community Land Model Version 5: Description of New Features, Benchmarking, and Impact of Forcing Uncertainty. *J. Adv. Model Earth Syst*. **11**, 4245–4287 (2019).
74. Pan, S. et al. Responses of global terrestrial evapotranspiration to climate change and increasing atmospheric CO_2 in the 21st century. *Earth's Future* **3**, 15–35 (2015).
75. Jinxun, L. et al. Terrestrial ecosystem modeling with ibis: progress and future vision. *J. Res. Ecol*. **13**, 2–16 (2022).
76. Jain, A. K. & Yang, X. Modeling the effects of two different land cover change data sets on the carbon stocks of plants and soils in concert with CO_2 and climate change. *Glob. Biogeochem. Cycles* **19**, GB2015 (2005).
77. Delire, C. et al. The Global Land Carbon Cycle Simulated With ISBA-CTRIP: Improvements Over the Last Decade. *J. Adv. Modeling Earth Syst*. **12**, e2019MS001886 (2020).
78. Reick, C. H., Raddatz, T., Brovkin, V. & Gayler, V. Representation of natural and anthropogenic land cover change in MPI-ESM. *J. Adv. Modeling Earth Syst*. **5**, 459–482 (2013).
79. Best, M. J. et al. The Joint UK Land Environment Simulator (JULES), model description – Part 1: Energy and water fluxes. *Geoscientific Model Dev*. **4**, 677–699 (2011).
80. Clark, D. B. et al. The Joint UK Land Environment Simulator (JULES), model description – Part 2: Carbon fluxes and vegetation dynamics. *Geoscientific Model Dev*. **4**, 701–722 (2011).
81. Smith, B., Prentice, I. C. & Sykes, M. T. Representation of Vegetation Dynamics in the Modelling of Terrestrial Ecosystems: Comparing Two Contrasting Approaches within European Climate Space. *Glob. Ecol. Biogeogr*. **10**, 621–637 (2001).
82. Stocker, B. D. et al. Multiple greenhouse-gas feedbacks from the land biosphere under future climate change scenarios. *Nat. Clim. Change* **3**, 666–672 (2013).
83. Krinner, G. et al. A dynamic global vegetation model for studies of the coupled atmosphere-biosphere system: DVGM FOR COUPLED CLIMATE STUDIES. *Global Biogeochem. Cycles* **19**, GB1015 (2005).
84. Woodward, F. I., Smith, T. M. & Emanuel, W. R. A global land primary productivity and phytogeography model. *Glob. Biogeochemical Cycles* **9**, 471–490 (1995).
85. Ito, A. Changing ecophysiological processes and carbon budget in East Asian ecosystems under near-future changes in climate: implications for long-term monitoring from a process-based model. *J. Plant Res*. **123**, 577–588 (2010).
86. Zhu, Z. et al. Attribution of seasonal leaf area index trends in the northern latitudes with "optimally" integrated ecosystem models. *Glob. Change Biol*. **23**, 4798–4813 (2017).
87. Wei, H. et al. The Strategic Random Search (SRS) – A new global optimizer for calibrating hydrological models. *Environ. Model. Softw*. **172**, 105914 (2024).
88. Ribes, A., Planton, S. & Terray, L. Application of regularised optimal fingerprinting to attribution. Part I: method, properties and idealised analysis. *Clim. Dyn*. **41**, 2817–2836 (2013).
89. Eyring, V. et al. Overview of the Coupled Model Intercomparison Project Phase 6 (CMIP6) experimental design and organization. *Geosci. Model Dev*. **9**, 1937–1958 (2016).
90. Allen, M. R. & Tett, S. F. B. Checking for model consistency in optimal fingerprinting. *Clim. Dyn*. **15**, 419–434 (1999).
91. Gu, X. et al. Attribution of Global Soil Moisture Drying to Human Activities: A Quantitative Viewpoint. *Geophys. Res. Lett*. **46**, 2573–2582 (2019).
92. Douville, H., Ribes, A., Decharme, B., Alkama, R. & Sheffield, J. Anthropogenic influence on multidecadal changes in reconstructed global evapotranspiration. *Nat. Clim. Change* **3**, 59–62 (2013).
93. Wei, H. et al. Direct vegetation response to recent CO_2 rise shows limited effect on global streamflow. Zenodo. https://doi.org/10.5281/zenodo.13908543 (2024).

Acknowledgements

Y.Q.Z. acknowledges the support by the National Key R&D Program of China (Grant No. 2022YFC3002804) and the National Natural Science Foundation of China (Grant No. 42330506 and 42361144709). Comments and suggestions from late Jianyu Liu have inspired us for using the optimal fingerprint method for global attribution of streamflow. We also acknowledge the TRENDY group responsible for the TRENDY models, as well as the modeling team that provided scenario simulations for TRENDY, and we thank Stephen Sitch, the leader of the TRENDY group, for providing the model output. We also thank Zhenwu Xu, Xuan Liu, Pengxin Jia, Ning Ma, Yi Wang and Yu Zhang for their suggestions and assistance.

Author contributions

Y.Q.Z. designed this study. H.S.W. conducted modelling, data analysis and figure plotting. Q.H. and H.S.W. collated datasets. Y.Q.Z. and H.S.W. wrote the first version of paper. J.X. provided considerable inputs for data analysis and guidance of modelling experiments. H.S.W., Y.Q.Z., J.X., F.C., J.K.L., Q.H., and C.M.L. contributed to discussion and interpretations of he results and writing the paper.

Competing interests

The authors declare no competing interests.

Additional information

Supplementary information The online version contains supplementary material available at https://doi.org/10.1038/s41467-024-53879-x.

Correspondence and requests for materials should be addressed to Yongqiang Zhang or Jun Xia.

Peer review information *Nature Communications* thanks the anonymous reviewers for their contribution to the peer review of this work. A peer review file is available.

Terms and Conditions

Springer Nature journal content, brought to you courtesy of Springer Nature Customer Service Center GmbH (“Springer Nature”).
Springer Nature supports a reasonable amount of sharing of research papers by authors, subscribers and authorised users (“Users”), for small-scale personal, non-commercial use provided that all copyright, trade and service marks and other proprietary notices are maintained. By accessing, sharing, receiving or otherwise using the Springer Nature journal content you agree to these terms of use (“Terms”). For these purposes, Springer Nature considers academic use (by researchers and students) to be non-commercial.
These Terms are supplementary and will apply in addition to any applicable website terms and conditions, a relevant site licence or a personal subscription. These Terms will prevail over any conflict or ambiguity with regards to the relevant terms, a site licence or a personal subscription (to the extent of the conflict or ambiguity only). For Creative Commons-licensed articles, the terms of the Creative Commons license used will apply.
We collect and use personal data to provide access to the Springer Nature journal content. We may also use these personal data internally within ResearchGate and Springer Nature and as agreed share it, in an anonymised way, for purposes of tracking, analysis and reporting. We will not otherwise disclose your personal data outside the ResearchGate or the Springer Nature group of companies unless we have your permission as detailed in the Privacy Policy.
While Users may use the Springer Nature journal content for small scale, personal non-commercial use, it is important to note that Users may not:

1. use such content for the purpose of providing other users with access on a regular or large scale basis or as a means to circumvent access control;
2. use such content where to do so would be considered a criminal or statutory offence in any jurisdiction, or gives rise to civil liability, or is otherwise unlawful;
3. falsely or misleadingly imply or suggest endorsement, approval , sponsorship, or association unless explicitly agreed to by Springer Nature in writing;
4. use bots or other automated methods to access the content or redirect messages
5. override any security feature or exclusionary protocol; or
6. share the content in order to create substitute for Springer Nature products or services or a systematic database of Springer Nature journal content.

In line with the restriction against commercial use, Springer Nature does not permit the creation of a product or service that creates revenue, royalties, rent or income from our content or its inclusion as part of a paid for service or for other commercial gain. Springer Nature journal content cannot be used for inter-library loans and librarians may not upload Springer Nature journal content on a large scale into their, or any other, institutional repository.
These terms of use are reviewed regularly and may be amended at any time. Springer Nature is not obligated to publish any information or content on this website and may remove it or features or functionality at our sole discretion, at any time with or without notice. Springer Nature may revoke this licence to you at any time and remove access to any copies of the Springer Nature journal content which have been saved.
To the fullest extent permitted by law, Springer Nature makes no warranties, representations or guarantees to Users, either express or implied with respect to the Springer nature journal content and all parties disclaim and waive any implied warranties or warranties imposed by law, including merchantability or fitness for any particular purpose.
Please note that these rights do not automatically extend to content, data or other material published by Springer Nature that may be licensed from third parties.
If you would like to use or distribute our Springer Nature journal content to a wider audience or on a regular basis or in any other manner not expressly permitted by these Terms, please contact Springer Nature at

onlineservice@springernature.com